# Demonstration of $MgCr_{2-x}Mn_xO_4$ spinel oxide cathodes in high voltage Mg batteries

*Evelyna Wang[1]*, Ritesh Uppuluri[1,2], Bob Jin Kwon[1], Erik Sarnello[1,3], Noel Leon[1], Zhenzhen Yang[1], Saul H. Lapidus[1,3], Kenneth R. Poeppelmeier[2], Baris Key[1]**

AUTHOR ADDRESS

[1]Chemical Sciences and Engineering Division, Argonne National Laboratory,

Lemont, Illinois 60439

[2]Department of Chemistry, Northwestern University,

Evanston, Illinois 60208

[3]X-ray Science Division, Advanced Photon Source Argonne National Laboratory,

Lemont, Illinois 60439

AUTHOR INFORMATION

**Corresponding Author**

* Evelyna Wang, evelyna.wang@anl.gov

*Baris Key, bkey@anl.gov

KEYWORDS

Mg batteries, Electrochemistry, Energy Storage, Spinel Oxides, Mg anode

ABSTRACT

Solid-solution oxide spinels with high redox voltages and facile $Mg^{2+}$ mobility have been identified as promising candidates for practical, high voltage cathodes in Mg batteries. In this work, we discuss the development of $MgCr_{2-x}Mn_xO_4$ [x = 0.5, 1, 1.2] solid solution spinel oxides as a cathode material and their electrochemical performance paired with a Mg anode in a full cell. This work presents the first demonstration of full cells with these materials. Mg-Cr-Mn spinel oxides with varying Cr and Mn contents were synthesized using alternative synthetic routes for optimal electrochemical performance. High-resolution synchrotron powder X-ray diffraction (PXRD), solid-state nuclear magnetic resonance (NMR) spectroscopy, and electron microscopy showed that these different synthetic routes resulted in changes in structures and particle morphologies, which in turn affect the electrochemical performance. Particularly, the urea co-precipitation synthetic route resulted in high surface area particles that enabled lower overpotentials and increased discharge capacity. The high surface area also resulted in expedited structural degradation caused by irreversible migration of $Mg^{2+}$ into normally vacant 16c sites in the spinel lattice. This structural degradation was lessened by using a hydrosauna-urea synthesis method which decreased the Mg/Mn inversion ratio while retaining high surface area particles with good cycling performance. Our findings highlight the necessity for high surface area or nanostructured spinel oxide cathodes with minimized Mg-Mn inversion to enable spinel oxide cathodes in Mg full cells.

*Introduction*

Non-aqueous Mg batteries are a class of next generation batteries that promise high energy densities as an alternative to Li-ion batteries [1, 2]. Materials discovery and development over the past decades have attempted to deliver suitable electrodes to fulfill this promise [3, 4]. For instance, reversible $Mg^{2+}$ ion intercalation has been demonstrated using sulfide-based cathodes [5, 6]. However, sulfide-based cathodes operate at low potentials (~ 1 V vs $Mg/Mg^{2+}$), thereby limiting their practical application. Theoretical works have suggested the feasibility of high voltage oxide cathodes [7-9]. As such, a whole suite of studies has focused on understanding and identifying optimal high voltage oxide cathodes in Mg batteries [10-16].

In particular, many of these works have focused on spinel oxide structures and the challenges with $Mg^{2+}$ (de)intercalation. First, Kim et al. demonstrated the intercalation of $Mg^{2+}$ into $Mn_2O_4$, however the high activation energy of $Mg^{2+}$ migration limited reversibility [11]. Subsequent studies then found that inversion between $Mg^{2+}$ and $Mn^{2+}$ ions within the $MgMn_2O_4$ spinel structure led to an increase in the cation migration barrier and affects reversibility [12, 13]. The Mg/Mn inversion could also be adjusted with synthetic conditions, for instance Bayliss et al. showed lowered inversion with low temperature annealing [13]. In parallel, investigations into $Mg^{2+}$ intercalation in $MgCr_2O_4$ was also explored due to the relatively facile $Mg^{2+}$ mobility as well as increased inversion stability, however, the high potentials for Cr redox as well as the instability of $Cr^{4+}$ presented additional challenges in developing Cr- based spinel oxide cathodes [17]. To leverage the advantages and mitigate challenges of the individual Mn- or Cr- spinel oxides, a solid solution $MgMnCrO_4$ was then proposed by Kwon et al. [14]. Reversible (de)intercalation of $Mg^{2+}$ in the solid-solution $MgMnCrO_4$ was clearly observed electrochemically and confirmed through XRD, XAS, and microscopy [14]. The solid solution combined the redox activity of Mn with the

relatively low migration barriers and added inversion stability due to the Cr. Figure 1 shows the mixed spinel oxide crystal structure and the Mg-Mn inversion, as well as $Mg^{2+}$ mobility.

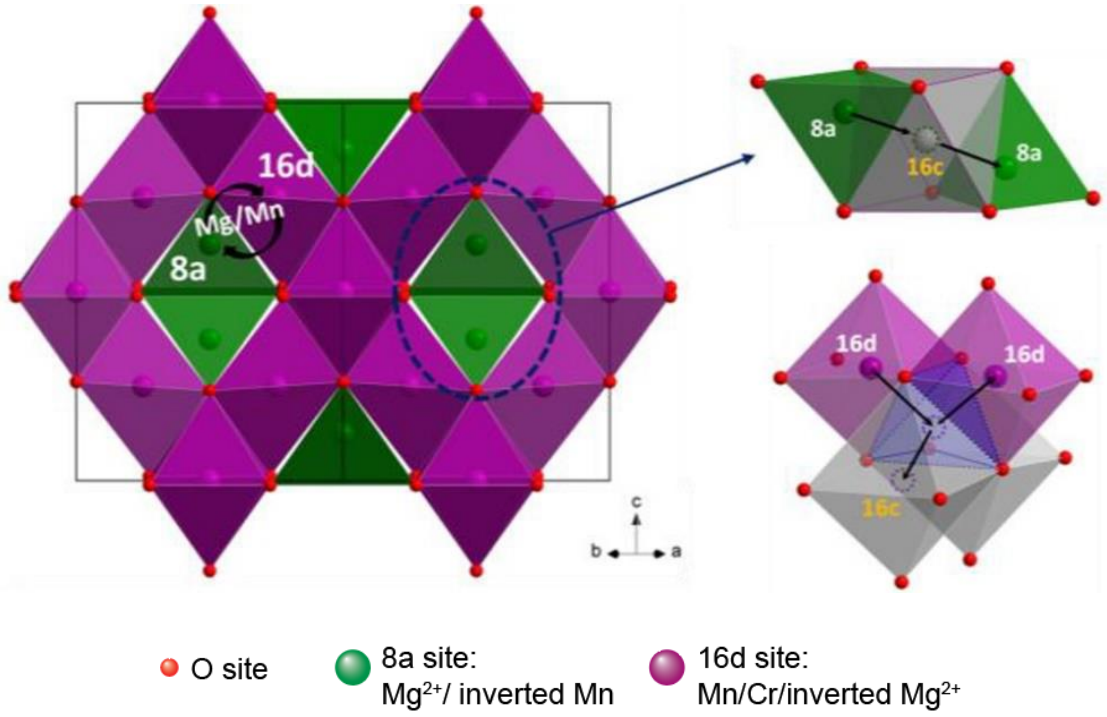


Figure 1: $MgCr_{2-x}Mn_xO_4$ solid solution spinel crystal structure with Mg-Mn inversion illustrated by the $Mn^{2+}$ (16d) – $Mg^{2+}$ (8a) exchange. The diffusion of $Mg^{2+}$ (8a) is depicted on the right top schematic, whereby the ions hop through the normally vacant 16c sites. Inverted $Mg^{2+}$ ions (16d) may migrate to neighboring 16d sites or 16c sites, as depicted on the right bottom schematic. Reproduced from [15]. Copyright [2021] American Chemical Society.

Detailed operando XRD studies were performed by Yin et al. to understand the cation redistributions during cycling within the solid-solution $MgCrMnO_4$ spinel oxide cathode [15]. They observed that the inverted Mn directly affects the $Mg^{2+}$ hopping, leading to irreversible migration of $Mg^{2+}$ into normally vacant sites. The ion migration caused by inversion resulted in voltage hysteresis and irreversible structural evolution with cycling, highlighting the importance

of minimizing Mg/Mn inversion in spinel oxide cathodes. A tailored inversion-free spinel oxide was then prepared by increasing the composition of Cr, resulting in a $MgCr_{1.5}Mn_{0.5}O_4$ cathode material with decreased overpotentials and hysteresis [18].

In addition to cathode development, considerable progress in Mg/Mg-ion battery research has also been made toward identifying compatible electrolytes [19, 20]. An ideal electrolyte is stable at the spinel oxide cathode redox potentials while also enabling homogeneous electrodeposition and dissolution at the Mg anode [21, 22]. Furthermore, electrolytes require chemical stability against the breakdown of solvent or solvated ion complexes. For Mg electrolytes to meet all the criteria, a custom Mg salt anion is required. Therefore, a highly electron-deficient and weakly coordinating anion salt was designed and assessed by Lau et al. [23]. They found that their novel perfluoroalkoxyaluminate (TPFA) anion limited the reductive decomposition during Mg plating.

Building upon the previous studies on $MgCrMnO_4$ spinel oxide cathodes and electrolyte systems, we aim to demonstrate their performance in full cells, paired with Mg anodes. To the best of our knowledge, this is the first demonstration of solid-solution spinel cathodes in a full cell configuration. Previous studies utilized carbon anodes, which served as high-surface area capacitive counter electrodes and were used to solely investigate the spinel oxide performance [13-15, 18]. Previous studies have also used a variety of alternative Mg anode materials [24], however these alternative anode materials would decrease the operating voltage window of a Mg cell.

Here, we evaluated the electrochemical performance of $MgCr_{2-x}Mn_xO_4$ spinel oxide cathodes prepared using conventional and novel synthetic routes cycled against Mg foil anodes. We found that the urea co-precipitation method resulted in a high-surface area cathode material, which led to improved electrochemical full cell performance despite higher Mg/Mn inversion ratios. We evaluated three compositions of $MgCr_{2-x}Mn_xO_4$ [x = 0.5, 1, 1.2]; we hypothesized that

an increase in the Mn content would increase the capacity, while an increase in Cr content would increase the transport of $Mg^{2+}$ within and the inversion stability of the spinel oxide structure. Following cycling, we performed detailed characterization using synchrotron XRD and solid-state NMR. We observed structural changes caused by Mg-ion migration and an increase in the cell impedance with cycling. These effects are attributed to both the higher inversion ratios as well as the high-surface area which exacerbated the structural evolution.

*Methods*

Materials: Magnesium acetate tetrahydrate ($Mg(CH_3COO)_2 \cdot 4H_2O$, Sigma-Aldrich), chromium acetate hydroxide ($Cr_3(CH_3CO_2)_7(OH)_2$, Sigma-Aldrich), manganese acetate dihydrate ($Mn(CH_3COO)_3 \cdot 4H_2O$, Sigma-Aldrich) were used as precursor materials. Citric acid ($C_6H_8O_7$, Sigma-Aldrich), Magnesium nitrate hexahydrate ($Mg(NO_3)_2 \cdot 6H_2O$, Sigma Aldrich), Chromium nitrate (Sigma Aldrich), Manganese nitrate ($Mn(NO_3)_2$, Sigma Aldrich), urea ($CO(NH_2)_2$, Sigma Aldrich), sodium hydroxide solution (1 M NaOH aqueous, Sigma Aldrich, and ethylene glycol ($(CH_2OH)_2$, Sigma Aldrich).

Synthesis: $MgCr_{2-x}Mn_xO_4$ [x = 0.5, 1, 1.2] solid-solution spinel oxides were prepared via three different synthetic routes: (1) polymerized complex sol-gel method, (2) topochemical transformation from layered double hydroxide precursors, and (3) homogenous co-precipitation of metal nitrates using urea. The polymerized complex sol-gel method has been previously used with spinel oxides [25]; esterification of citric acid and ethylene glycol can promote intimate mixing of acetate precursors. Samples were then annealed at 450°C followed by a higher temperature anneal at 800°C. Topochemical dehydration of layered double hydroxide precursors to spinel oxides have been previously demonstrated [26-28]. In this work, the Mg-Cr-Mn layered double hydroxides were prepared via co-precipitation of metal nitrate salts (in stoichiometric quantities) dissolved in

aqueous NaOH (1 M). The precipitate was then dried at 60°C, followed by annealing at 800°C for 24 hours to form a mixture of spinel oxide and precursor oxides; the latter could be removed by acid treatment with hydrochloric acid (1 M). The layered double hydroxide method has been previously demonstrated to synthesize spinel oxides with low inversion [27, 28]. The third method, homogenous urea co-precipitation, has also been demonstrated for spinel oxide synthesis [29, 30]. For the urea co-precipitation method used in this work, an aqueous solution of nitrate salts and an equivalent amount of urea was stirred at 90°C under alkaline conditions. The resultant gel was calcined at 450°C for 1 hour, then at 700°C for 24 hours. A hydro-sauna method was also tested with the urea co-precipitation synthesis. Hydro-sauna methods refer to calcination of precursors in humid environments with controlled water vapor and has been utilized to prepare phase-pure perovskites [31]. For this work, the gel prepared by the urea co-precipitation method was calcined in a humid environment at 450°C (24 h) followed by cooling to 150 °C (15 °C/min) and natural cooling to room temperature.

We also tested spinel oxides synthesized via conventional aqueous sol-gel method. The methods are as described in previous literature by Kwon et al. [18]. As we will discuss later, we also assessed electrode laminates made with these conventional sol-gel methods after ball-milling to decrease the particle size. The spinel oxide powders were milled with stainless steel balls and a high-energy SPEX mixer (BM-450) for 30 min prior to laminate preparation.

Cell assembly and electrochemical testing: Cathode powders were mixed into slurries and cast onto stainless steel foil to make electrode laminates. A ratio of 60 weight percent active material, 20% carbon conductive additive (C45, TIMCAL) and 20% PVDF binder (dissolved in NMP) was used. The electrodes were dried under vacuum at 80 °C overnight, then punched into discs (diameter = 3/8 in). Active material loading was between 1.5-3 mg $cm^{-2}$. Coin cells were

assembled in an Ar-filled glovebox using the prepared cathodes, Mg foil as the anode (thickness = 0.25 mm, diameter = 15 mm), and Whatman glass fiber separators. The Mg anodes were mechanically polished in the glove box until shiny to remove oxidized surface species; see Figure S1. The electrolyte used was 0.1 M Mg $[TPFA]_2$ ($[TPFA]^- = [(Al(OC(CF_3)_3)_4)^-]$) in triglyme (60 µL). The $Mg[TPFA]_2$ salt was prepared at scale at the Materials Engineering and Research Facility (MERF) at Argonne, following procedures previously published and resulting in high purity compounds ($Li^+$ and $Cl^-$ contaminants < 98 ppm) after recrystallization [23]. Electrolytes were prepared in an Ar-filled glovebox. The triglyme was purchased from Sigma Aldrich and distilled under vacuum from NaH [23]. The electrolyte water content was [< 20] ppm.

Cells were cycled at a C/50 rate with upper and lower voltage cut-off of 4.0 V and 0.5 V vs $Mg/Mg^{2+}$, respectively, and a 100 mAh $g^{-1}$ capacity limit; this capacity cut-off will be discussed in the results. Cells were cycled at elevated temperature (95°C) using a MACCOR battery cycler. The theoretical capacities used to calculate C-rate were estimated based solely on the Mn redox, whereby $MgCrMnO_4$ has a theoretical capacity of 280 mAh $g^{-1}$.

Characterization: Coin cells were disassembled in an Ar-filled glovebox and prepared for ex-situ characterization. Solid-state magic-angle-spinning NMR was performed on a 500 MHz (T) Bruker Avance III spectrometer. The cathodes were packed into a 3.2 mm zirconia rotor. Samples were spun at 20 kHz and measured using a hahn-echo pulse sequence with recycle delays of 0.1 s and pulse width 3 µs. SEM of the samples were measured using a JEOL JCM-6000Plus benchtop SEM. Samples were prepared under ambient conditions. High-resolution ex-situ XRD was performed at the 11-BM beamline at the Advanced Photon Source, Argonne National Laboratory. Samples were packed in Kapton capillaries. Spectra were refined using the Rietveld method using Topaz software and GSAS-II.

*Results*

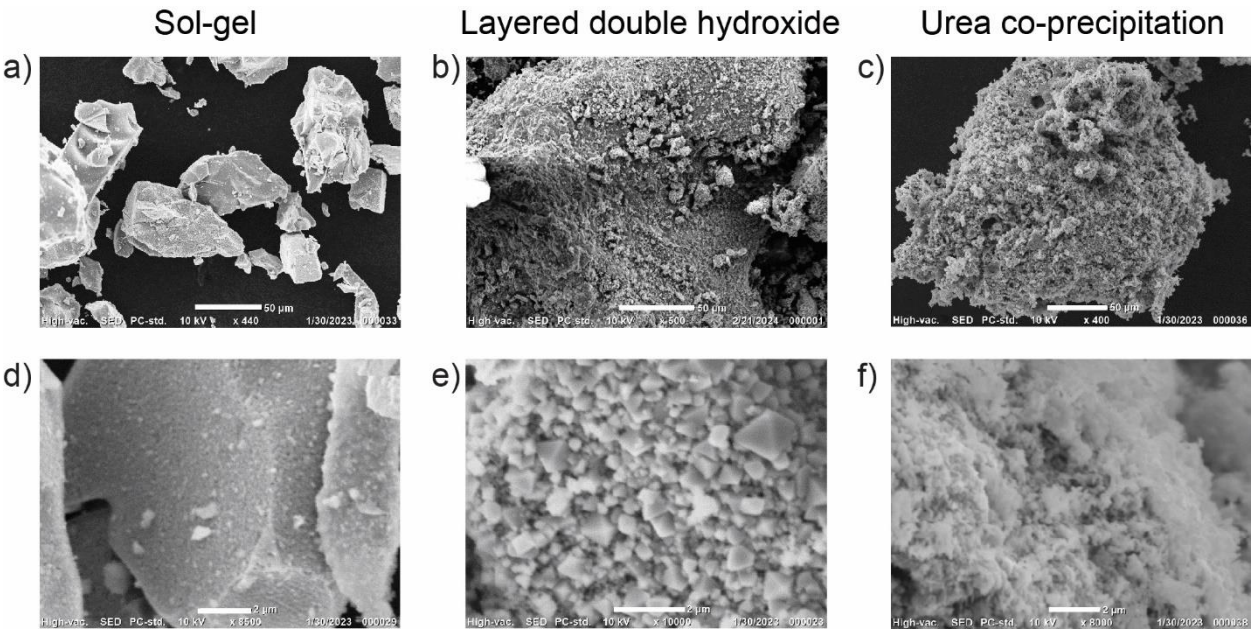


Figure 2: SEM images of the pristine $MgCr_{1.5}Mn_{0.5}O_4$ spinel oxide compounds synthesized via sol-gel (a, d), layered double hydroxide (b, e), and urea co-precipitation (c, f). Scale bar in (a-c) is 50 µm. Scale bar in (d-f) is 2 µm.

We successfully explored various synthetic methods to obtain the Mg spinel oxide powders. Figure 2 shows the SEM images of the $MgCr_{1.5}Mn_{0.5}O_4$ spinel cathode materials prepared using aqueous sol-gel reaction, layered double-hydroxide precursors, and urea co-precipitation. The polymerized complex method however did not result in improved cationic inversion over the conventional aqueous sol-gel method, used in previous literature [14]; for the rest of this work, the sol-gel $MgCr_{2-x}Mn_xO_4$ samples refer to those synthesized via conventional aqueous methods. The aqueous sol-gel method resulted in particles 10-50 µm in diameter. The large and crystalline particles from the sol-gel method were likely a result of a post anneal step; these samples were post annealed at 350°C in air for a month to decrease the Mg/Mn inversion which may have led to particle aggregation. Smaller particles (0.5-2 µm diameter) were obtained

using a topochemical synthetic route with layered double-hydroxide precursors (LDH). These particles also had a faceted morphology. By contrast, the urea co-precipitation synthesis resulted in a non-particulate, porous morphology. Estimation from the SEM image suggests pore diameters ranging from submicron to a few microns, as shown in Figure S2. Urea is well known as a non-surfactant templating agent for producing particles of porous morphology and has previously been utilized to prepare mesoporous silica and titania by sol-gel reactions that resulted in enhanced surface area. [32, 33]

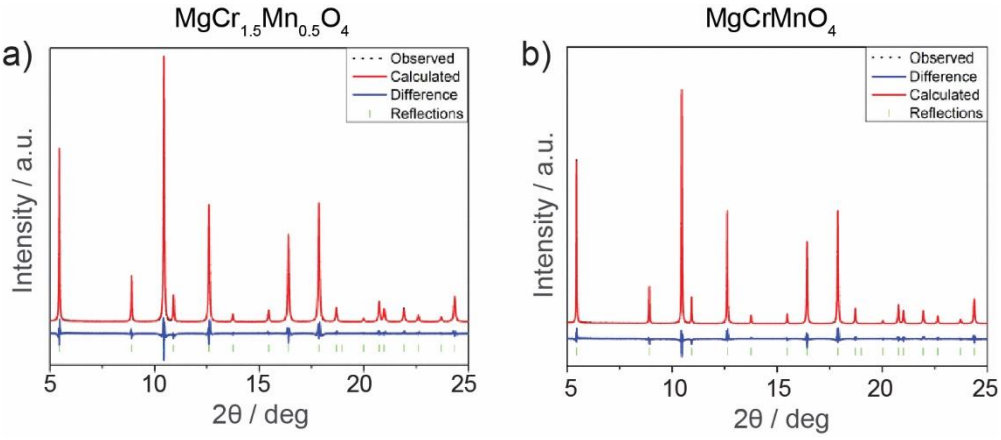


Figure 3: XRD spectra for (a) the pristine $MgCr_{1.5}Mn_{0.5}O_4$ and (b) $MgCrMnO_4$ spinel oxides synthesized via urea co-precipitation.

The XRD data of the pristine $MgCr_{1.5}Mn_{0.5}O_4$ spinel cathodes synthesized using the urea co-precipitation method were measured to compare the Mg-Mn inversion. Rietveld refinement was used to determine the inversion. The inversion ratio was 13.5% for the $MgCr_{1.5}Mn_{0.5}O_4$ composition and 18.9% for $MgCrMnO_4$ composition. Compared to literature values of 10% inversion for $MgCrMnO_4$ or even defect-free $MgCr_{1.5}Mn_{0.5}O_4$ spinel oxides [14, 18], the new urea synthetic routes resulted in higher inversion ratios than conventional sol-gel synthesis methods.

Figure S3 and S4 shows the XRD spectra for pristine $MgCrMnO_4$ and $MgCr_{1.5}Mn_{0.5}O_4$ spinel oxide prepared using the layered double hydroxide precursor route. Although the sample was a phase-pure compound, some mismatches in peak intensities in Rietveld refinement were observed, which could be attributed to stacking faults, vacancies, and/or compositional heterogeneity. Additionally, we were able to synthesize the metastable $MgCr_{0.8}Mn_{1.2}O_4$, which has the highest amount of Mn in the lattice while maintaining the desired cubic symmetry. For both citrate sol-gel and urea co-precipitation methods, this composition resulted in an inversion of ~20%, as calculated from the XRD spectra included in Figure S5. The $MgCr_{0.8}Mn_{1.2}O_4$ spinel oxide prepared via layered double hydroxide methods did not result in a phase-pure sample.

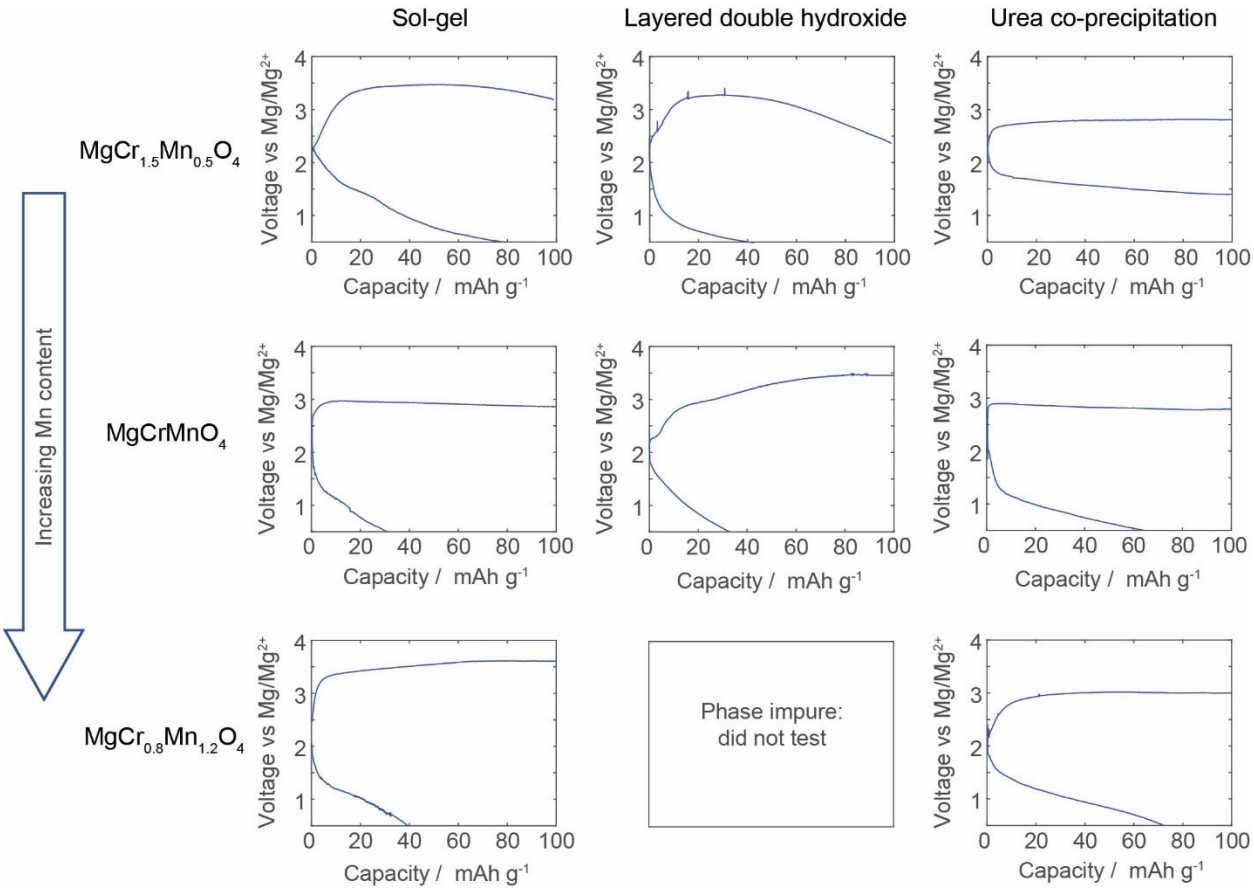

Figure 4: First cycle voltage versus specific capacity plots for Mg full cells with spinel oxide cathodes varying synthetic route and composition. The lower cut-off potential was set to 0.5 V vs $Mg/Mg^{2+}$.

Figure 4 shows the electrochemical data for full Mg spinel oxide cells with varying compositions and synthetic routes. Only the first cycle data is shown for clarity. In addition, cells were cycled with a 100 mAh $g^{-1}$ limit; this was due to the severe overcharge behavior observed for the first cycle before reaching a 4.0 V cut-off potential as shown in Figure S7. Across all the compositions evaluated, the urea co-precipitation method produced the best electrochemical results; these cells exhibited the lowest overpotential during both charge and discharge. The urea synthesis also increased the discharge capacity, in other words increased reinsertion of Mg into the cathode. The urea synthesis method also produced the best half-cell performance, shown in Figure S5. In particular, the cell with the highest discharge capacity and lowest overpotentials was obtained with the $MgCr_{1.5}Mn_{0.5}O_4$ composition synthesized via urea co-precipitation.

For both the urea synthesis and the sol-gel synthesis, increasing the Mn content resulted in a decrease in discharge capacity, despite the increased amount of redox active Mn. Therefore, we associated the decreases in discharge capacity to the increase in inversion with increasing Mn content, which can decrease $Mg^{2+}$ transport and drive increases in overpotential. The LDH synthesis resulted in the lowest capacity cells during discharge across all compositions, suggesting poor reinsertion of the Mg-ions into the cathode. The observed faceted morphology in LDH synthesized cathodes from Figure 2e, therefore appears to worsen the cell performance despite seemingly higher surface area compared to the sol-gel synthesized samples. This suggests certain facets may result in higher Mg (de)insertion activation energies and can explain the increased

overpotentials observed for LDH cathode cells. The $MgCr_{0.8}Mn_{1.2}O_4$ LDH synthesized cathode was phase impure and therefore was not included in this study.

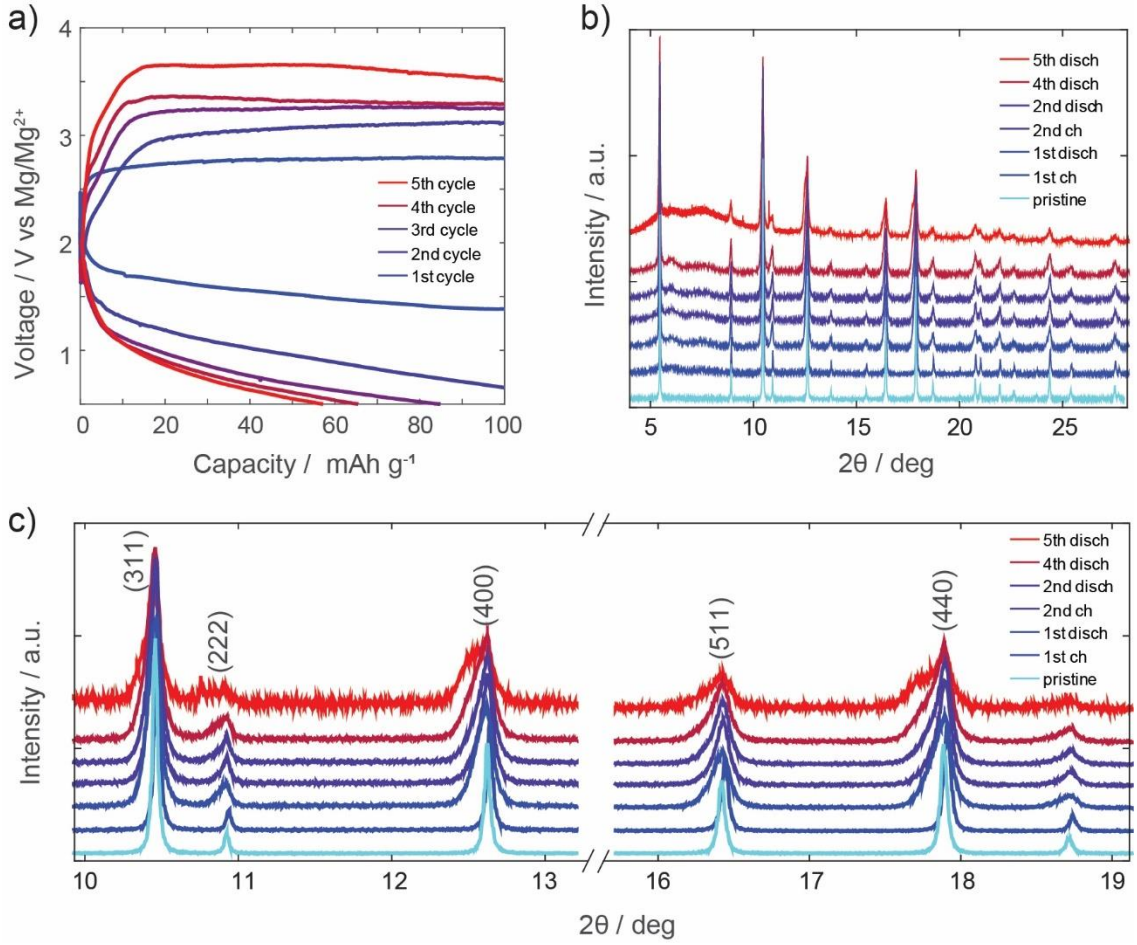


Figure 5: a) Voltage versus specific capacity plot for the best performing cathode: $MgCr_{1.5}Mn_{0.5}O_4$ with urea co-precipitation synthesis, b) XRD spectra for the cell measured at the end of charge or discharge for the 1st, 2nd, 4th, and 5th cycles, and c) same XRD spectra focusing on select reflections.

Figure 5a shows further cycling of the best performing cathode: the $MgCr_{1.5}Mn_{0.5}O_4$ urea co-precipitation synthesized cathode. There is a rapid increase in overpotential within a few cycles; the charge potential increases by nearly 500 mV by the 3rd cycle. The discharge capacity also

decreases rapidly, dropping to 85 mAh $g^{-1}$ by the 3rd cycle and 55 mAh $g^{-1}$ by the 5th cycle. Although there is a decay in performance within the first 4 cycles, the electrochemical performance is improved compared to cells with sol-gel synthesized $MgCr_{1.5}Mn_{0.5}O_4$ cathodes, shown in Figure S11. In addition, we tested the cycling behavior of a Mg foil -Mg foil symmetric cell to investigate the Mg plating potentials as shown in Figure S12. The Mg plating potentials are affected by the formation of SEI species as well as the desolvation energies for $Mg^{2+}$ ions. We observe a slow increase in the plating potential with increasing cycle number, which may be a result of accumulating SEI species with increasing cycle number. The increase in the Mg plating potentials however is slower than the increase in overpotentials in a full cell, suggesting that the overpotential growth in full cells was mostly caused by the cathode reactions. The Mg plating potential instabilities can also help explain the sloping voltage profiles observed in the first charge for several of the Mg full cells shown in Figure 4. The Mg plating potential instabilities in our system is beyond the scope of this work, however, has been previously discussed in literature studies focusing on Mg anode surface reactions [34]. Fluctuations in the voltage curve can occur due to changes in the anode surface area during stripping,[35] indicating that our Mg anode does not have uniform plating/stripping behavior in this electrolyte and further optimization is required for anode compatibility.

Cathodes were harvested for ex-situ characterization following the 1st, 2nd, 4th, and 5th cycles. Figure 5b shows the stacked XRD spectra comparing the effects of cycling. We observe a shifting of the XRD peaks from the pristine to the first charge, indicating Mg removal, followed by a shifting back of the XRD peaks after discharge, indicating Mg insertion. This lattice breathing has been previously linked to electrochemical Mg removal and insertion, as opposed to proton insertion [14,18, 36]. Additionally, the appearance of a new phase is observed immediately after

the 1st discharge; the new phase appears as a shoulder peak and can be seen more clearly in Figure 5c. This phase is not observed after the first charge where $Mg^{2+}$ ions were removed; however, it is observed after the second charge. This indicates that this phase forms during Mg insertion on the first discharge and that it is irreversible as subsequent Mg removal on the second charge does not remove this phase. Furthermore, this phase continues to accumulate with each cycle.

**Table 1**. Extracted parameters from Rietveld refinement for the XRD data of the cycled $MgCr_{1.5}Mn_{0.5}O_4$ cathode shown in Figure 5.

| Sample | Lattice Parameter (Å) | | Inversion (%) | Fraction of phase (%) | | Mg 16c site occupancy in Phase 2 | Mg 8a site occupancy in Phase 2 |
|---|---|---|---|---|---|---|---|
| | Phase 1 | Phase 2 | | Phase 1 | Phase 2 | | |
| Pristine | 8.353 | - | 8.02 | 100 | 0 | - | - |
| 1st Disch | 8.358 | 8.400 | 8.02 | 70.68 | 29.32 | 0.296 | 0.642 |
| 2nd Disch | 8.359 | 8.400 | 8.02 | 69.28 | 30.72 | 0.283 | 0.676 |
| 4th Disch | 8.360 | 8.417 | 8.02 | 70.57 | 29.43 | 0.378 | 0.607 |
| 5th Disch | 8.360 | 8.435 | 8.02 | 65.82 | 34.18 | 0.550 | 0.560 |

Rietveld refinement of the ex-situ XRD data is shown in Table 1. The new phase, labeled phase 2, contains $Mg^{2+}$ occupying normally vacant 16c sites. Both fraction of the new phase and the occupancy of the 16c site within this phase increases with increasing cycling number. This phenomenon has been previously shown using operando XRD on these Mg-Cr solid-solution spinel oxides materials, whereby normally vacant 16c site exhibits some fractional occupancy during Mg reinsertion [15]. The inversion was kept constant throughout the refinement to decrease the number of refinement parameters. The inversion therefore represents the average inversion of

both phases; there may be changes to the degree of inversion within phase 1 and phase 2 with increasing cycle number.

This irreversible accumulation of $Mg^{2+}$ occupying the 16c sites correlates well with the decrease in electrochemical performance (i.e., overpotential and subsequent loss of capacity). The decay in performance is caused by a combination of both decreased $Mg^{2+}$ transport and decreased amount of available $Mg^{2+}$. Further cycling of the $MgCr_{1.5}Mn_{0.5}O_4$ urea cells resulted in severe impedance and minimal charge or discharge capacity, shown in Figure S13.

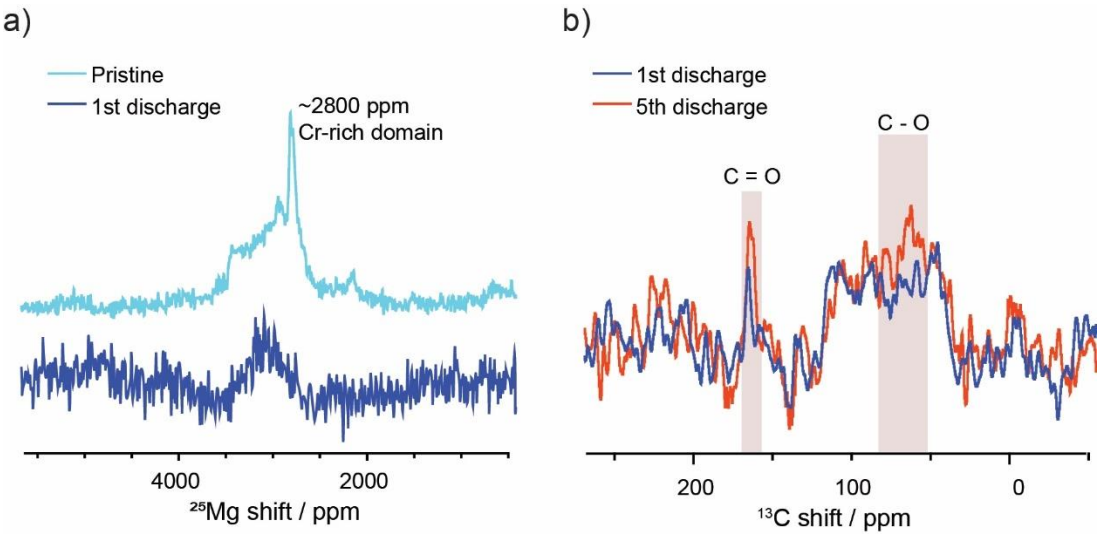


Figure 6: a) Ex-situ MAS $^{25}Mg$ NMR spectra comparing the pristine (cyan) $MgCr_{1.5}Mn_{0.5}O_4$ urea synthesized spinel oxide and after the first cycle (blue). The spectra are mass normalized. b) ex-situ MAS $^{13}C$ NMR spectra for the cycled $MgCr_{1.5}Mn_{0.5}O_4$ urea synthesized spinel oxide.

Existence of a chromium rich environment was observed in the $^{25}Mg$ NMR spectra shown in Figure 6a (cyan) for the $MgCr_{1.5}Mn_{0.5}O_4$, urea synthesis samples due to the high Cr content. Although the XRD spectra for this sample shown in Figure 3a, indicated phase purity, nano-domains of Cr-rich phases can exist and thus were detected via NMR. Interestingly, this Cr-rich domain is not observed in $MgCr_{1.5}Mn_{0.5}O_4$ synthesized via sol-gel methods [18]. Furthermore, this

Cr-rich domain disappears after the first cycle, suggesting activation of the Cr-redox at lower potentials than previously reported [14]. The Cr-rich phase however shows an irreversible activation and is not re-formed after re-insertion of the Mg. Although Mg cations coordinated to Cr-rich domains has been activated previously, insertion of $Mg^{2+}$ into the Cr-rich domain during discharge was not observed in our sample due to instability of the $Cr^{4+}$ charged state [13]. We do observe $Mg^{2+}$ inserted in the spinel framework after discharge from the mass normalized $^{25}Mg$ NMR spectra in Figure 6a, albeit not to the same Mg content as the pristine sample. Additionally, we used Electron Dispersive X-ray Spectroscopy (EDS) to quantify Mg, Cr, Mn, and O content and identify Mg electrochemical activity. This is summarized in Table S1. We observe an increase in the ratio of Mg to transition metal (Cr + Mn) going from a charged sample to a discharged sample, consistent with the structural activity probed via XRD.

Degradation of electrolyte on the cathode surface may also contribute to the overpotential increase with time and decay in electrochemical performance. An accumulation of electrolyte degradation species on the cathode surface, resulting in a cathode-electrolyte-interphase (CEI) layer, can increase the impedance and limit $Mg^{2+}$ ion insertion. An ex-situ $^{13}C$ MAS NMR measurement of the cycled cathode is shown in Figure 5b. Some organic growth of CEI is observed: the carbonyl peak at ~160 ppm and the C-O species at 60-80 ppm, increased slightly after 5 cycles compared to the 1st cycle. Overall, there are only minor accumulation of electrolyte breakdown products, which suggests some of the overpotential observed in Figure 5 is a result of CEI formation due to electrolyte breakdown while the majority can be attributed to the cathode structural changes with cycling.

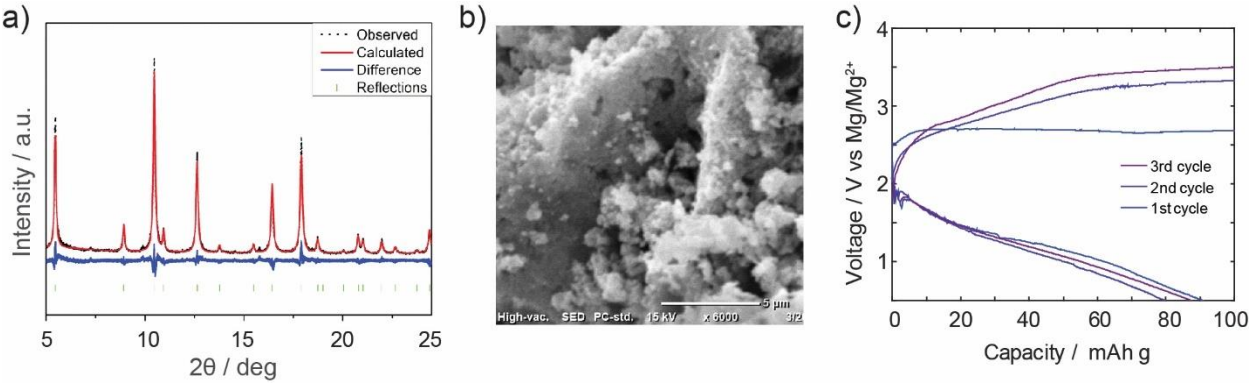


Figure 7: a) XRD spectra and b) SEM image of the pristine $MgCrMnO_4$ spinel oxide synthesized via hydrosauna methods using urea precursors, and c) first 3 cycles for the full cell with $MgCrMnO_4$, hydrosauna urea synthesized cathode.

Finally, we characterized and compared the electrochemical performance of $MgCrMnO_4$ spinel oxide prepared via a hydrosauna method using the urea co-precipitation method. Figure 7a shows the XRD spectra for the $MgCrMnO_4$ composition prepared via the hydrosauna-urea synthesis. Although the hydrothermal synthesis had lower peak intensities indicating less crystallinity, the Mg/Mn inversion ratio was lower compared to the high temperature urea synthesis shown in Figure 3b: Mg/Mn inversion ratio was 12.5%. The SEM image shown in Figure 7b indicates some of the porous morphology is retained. The $MgCr_{1.5}Mn_{0.5}O_4$ compound prepared by the hydrosauna method was biphasic, shown in Figure S6.

We observed electrochemical performance comparable to the higher temperature urea synthesis shown in Figure 5a. In fact, the decay in performance for the hydrosauna cathodes appeared mitigated; the capacity did not drastically decrease in the first three cycles. The biphasic $MgCr_{1.5}Mn_{0.5}O_4$ compound prepared by the hydrosauna-urea method also shows improved capacity retention, shown in Figure S14, compared to the normal urea synthesis.

*Discussion*

While the new synthetic routes were unable to decrease the extent of Mg/Mn inversion in Mg-Cr mixed spinel oxide cathodes, the urea synthesis method resulted in an increase in surface area. The high-surface area, in turn, led to the best performing Mg full cells to date. This suggests that surface area has a large effect on the rate and capacity, despite Mg/Mn inversion. Previous works optimizing Mg/Mg-ion battery high-voltage cathodes support this observation as they have focused on preparing porous and/or ultrasmall nanoparticulate materials [37-39]. This improves both the capacity as well as the rate capabilities. Kobayashi et al. demonstrated room-temperature operation of a nanoparticulate (< 2.5nm) cathode paired with a Mg-alloy anode, highlighting that nano-structuring and surface-area tailored cathodes can enable significantly improved electrochemistry [37]. However, similar to this work, their cells show rapid capacity fade within the first 5 cycles [37].

The urea co-precipitation method applied to synthesize Mg-Cr mixed spinel oxide cathodes has been used in other fields to control surface area and porosity in materials [32, 33, 40, 41]. Specifically, the urea co-precipitants led to higher pore volumes and specific area when compared to other co-precipitants used [40]. In catalysis, the increased surface area and porosity from the urea synthesis enabled improved redox performance for ethanol conversion and hydrogen selectivity [41]. In addition, other spinel oxides synthesized via the urea co-precipitation method were demonstrated to have high surface areas and nanoparticulate morphologies [30], again aligning with the observed morphologies for our urea co-precipitation synthesized Mg-Cr spinel oxide cathodes.

To further confirm the effect of surface area on electrochemical performance, we ball-milled the sol-gel cathode powders to decrease the particle size. After ball-milling, the particle sizes were

decreased to submicron in diameter, as shown in Figure S15. Using the milled cathode powder, we prepared electrode laminates and fabricated Mg full coin cells. We observed improvements in the cell overpotential, especially during charge, as well as a small increase in discharge capacity, shown in Figure S16. This supports both that the cathode surface area impacts the electrochemical performance in Mg full cells and that the porous morphology attained from the urea synthetic route resulted in even larger surface area increase.

The improvements to the electrochemistry enabled by the high surface area urea synthesis are short-lived due to the irreversible structural changes as shown in the ex-situ XRD in Figure 5c and summarized in Table 1. In addition, the discharge profiles for the high surface area urea synthesis cathodes also hint at the immediate irreversible structural changes. Whereas the voltage discharge profile for sol-gel synthesized cathodes shown in Figure 4 have two plateaus-like regions, the urea synthesized cathodes show only one discharge plateau-like region. Analysis from Yin et al. found that for conventional sol-gel synthesized spinel oxides, the first discharge plateau/process corresponds to the reversible reinsertion of Mg into the 8a sites, while the second plateau/process is attributed to an over-discharge, whereby $Mg^{2+}$ ions irreversibly insert and migrate into normally vacant 16c sites [15]. The absence of the two plateaus-like regions in the urea synthesis $MgCr_{1.5}Mn_{0.5}O_4$ cell suggests that the $Mg^{2+}$ insertion into 16c sites takes place immediately rather than as the second step. Interestingly, the ball-milled sol-gel synthesis also shows a smoothing of the two discharge processes, as seen in Figure S10, suggesting that an increase in surface area and/or the disorder introduced with ball-milling may also directly promote irreversible $Mg^{2+}$ migration. Furthermore, earlier studies found in literature have suggested a conversion mechanism whereby amorphous MgO is formed during the magnesiation of $MnO_2$ [42]. Due to the conversion mechanism, surface area effects were not the dominant factor affecting electrochemical

performance. For our work however, we did not observe any MgO at 26 ppm following $Mg^{2+}$ insertion into the Cr-Mn mixed spinel oxide as shown in the $^{25}Mg$ NMR spectra shown in Figure S17. This suggests that we have avoided the conversion reaction and that the sloping voltage profiles are likely indicative of irreversible ion migration. The Mg insertion into spinel oxides is consistent with previous theoretical and experimental studies [7-15].

Theoretical studies indicate that structural changes in spinel oxides during $Mg^{2+}$ insertion begin at the surface [43], therefore higher surface areas will result in increased change. The formation of a new phase in the urea synthesis spinel cathodes with cycling was an expedited but otherwise identical structural degradation to that presented by Yin et al. [15]. The high-surface area combined with even higher inversion ratios for the $MgCrMnO_4$ and the $MgCr_{0.8}Mn_{1.2}O_4$ urea synthesis cathodes resulted in even worse structural degradation, leading to high overpotentials on discharge and limited capacity. On the other hand, the $MgCrMnO_4$ synthesized via hydrosauna-urea methods shown in Figure 7c had a lower inversion ratio, which decreased the structural degradation caused by irreversible $Mg^{2+}$ migration, and thus outperformed the urea synthesis method of the same composition. Therefore, we did not change the fundamental challenges with Mg-ion spinel oxide materials when preparing them via a urea co-precipitation method. Instead, the improved electrochemical performance was strictly a result of an improved cathode design with high surface area when using the novel synthetic route. Furthermore, we have highlighted the irreversibility of Mg insertion into the spinel lattice during full cell discharge, as observed in both the dQ/dV plots and the cyclic voltammetry data shown in Figures S9 and S10, respectively. The role of synthesis processes and conditions in determining electrochemical performance of electrode materials, particularly in oxides, has been previously explored [44]. This opens possibilities for future work

in developing low-inversion spinel oxide cathode materials with morphological characteristics similar to the powders obtained from urea coprecipitation method reported here.

*Conclusion*

Electrochemical results in Mg full cells indicate improved performance for $MgCr_{2-x}Mn_xO_4$ cathodes synthesized via urea co-precipitation method over traditional sol-gel method. An increase in the surface area caused by the urea synthetic route enabled lower overpotentials and increased capacity. This emphasizes the importance of ion transport and conductivity in these spinel oxide materials as Mg-ion cathodes. However, the high surface area also resulted in expedited structural degradation, whereby $Mg^{2+}$ ions irreversibly migrate into normally vacant 16c sites. The structural changes decreased ionic mobility and caused a growth in overpotential during full cell cycling. This structural degradation was lessened when the spinel oxide cathodes were prepared using a hydrosauna-urea synthesis method with lower Mg/Mn inversion ratio. The hydrosauna-urea synthesis resulted in decreased Mg/Mn inversion while retaining the high surface area and thereby good electrochemical performance. In addition, the Mg $[TPFA]_2$ electrolyte used showed good stability against the high voltage spinel cathode, with limited accumulation of CEI. To the best of our knowledge, full cells testing of Mg-Cr-Mn spinel oxide cathodes have not been previously reported and is a significant milestone in high voltage Mg/Mg-ion battery field. This study opens an avenue in developing Mg full cells with spinel oxide cathodes and future work can be envisioned in synthesis of cathodes with high surface area and low Mg/Mn site inversion in the spinel lattice.

ASSOCIATED CONTENT

**Supporting Information:** additional XRD spectra, SEM images, and electrochemistry data.

AUTHOR INFORMATION

**Corresponding Author**

* Evelyna Wang, evelyna.wang@anl.gov

*Baris Key, bkey@anl.gov

ACKNOWLEDGEMENTS

The authors would like to acknowledge Emily Greenstein for experimental support with hydrosauna synthesis at Northwestern University. The authors also thank Krzysztof Pupek and Trevor Dzwiniel for the preparation of the electrolyte salt at the Materials Engineering and Research Facility at Argonne. This work was supported solely by the Joint Center for Energy Storage Research (JCESR), an Energy Innovation Hub funded by the U.S. Department of Energy, Office of Science, Basic Energy Sciences. The submitted manuscript has been created by UChicago Argonne, LLC, Operator of Argonne National Laboratory ("Argonne"). Argonne, a U.S. Department of Energy Office of Science laboratory, is operated under Contract No. DE-AC02-06CH11357. Use of the Advanced Photon Source at Argonne National Laboratory was supported by the U.S. Department of Energy, Office of Science, Office of Basic Energy Sciences, under Contract No. DE-AC02-06CH11357.

REFERENCES

[1] Levi, E.; Gofer, Y.; Aurbach, D. On the Way to Rechargeable Mg Batteries: The Challenge of New Cathode Materials. *Chem. Mater.* **2010**, 22, 860-868. DOI: 10.1021/cm9016497

[2] Muldoon, J.; Bucur, C. B.; Gregory, T. Quest for Nonaqueous Multivalent Secondary Batteries: Magnesium and Beyond. *Chem. Rev*. **2014**, 114, 11683-11720. DOI: 10.1021/cr500049y

[3] Rashad, M.; Asif, M.; Wang, Y.; He, Z.; Ahmed, I. Recent advances in electrolytes and cathode materials for magnesium and hybrid-ion batteries. *Ener. Stor. Mater.* **2020**, 25, 342-375. DOI: 10.1016/j.ensm.2019.10.004

[4] Niu, J.; Zhang, Z.; Aurbach, D.; Alloy Anode Materials for Rechargeable Mg Ion Batteries. *Adv. Ener. Mater.* **2020**, 10, 2000697. DOI: 10.1002/aenm.202000697

[5] Nguyen, D.-T.; Horia, R.; Eng, A. Y. S.; Song, S.-W.; Seh, Z. W. Material design strategies to improve the performance of rechargeable magnesium–sulfur batteries. *Mater. Horiz.* **2021**, 8, 830-853. DOI: 10.1039/D0MH01403F

[6] Wang, P.; Buchmeiser, M. R. Rechargeable Magnesium–Sulfur Battery Technology: State of the Art and Key Challenges. *Adv. Func. Mater.* **2019**, 29, 1905248. DOI: 10.1002/adfm.201905248

[7] Hannah, D. C.; Gautam, G. S.; Canepa, P.; Ceder, G. On the Balance of Intercalation and Conversion Reactions in Battery Cathodes. *Adv. Ener. Mater.* **2018**, 8, 1800379. DOI: 10.1002/aenm.201800379

[8] Liu, M.; Rong, Z.; Malik, R.; Canepa, P.; Jain, A.; Ceder, G.; Persson, K. A. Spinel compounds as multivalent battery cathodes: a systematic evaluation based on ab inition calculations. *Ener Environ. Sci.* **2015**, 8, 964-974. DOI: 10.1039/C4EE03389B

[9] Rong, Z.; Malik, R.; Canepa, P.; Gautam, G. S.; Liu, M.; Jain, A.; Persson, K.; Ceder, G. Materials Design Rules for Multivalent Ion Mobility in Intercalation Structures. *Chem. Mater.* **2015**, 27, 6016-6021. DOI: 10.1021/acs.chemmater.5b02342

[10] Sun, X.; Duffort, V.; Mehdi, L.; Browning, N. D.; Nazar, L. F. Investigation of the Mechanism of Mg Insertion in Birnessite in Nonaqueous and Aqueous Rechargeable Mg-Ion Batteries. *Chem. Mater.* **2016**, 28, 534-542. DOI: 10.1021/acs.chemmater.5b03983

[11] Kim, C.; Phillips, P. J.; Key, B.; Yi, T.; Nordlund, D.; Yu, Y.-S.; Bayliss, R. D.; Han, S.-D.; He, M.; Zhang, Z.; Burrell, A. K.; Klie, R. F.; Cabana, J. Direct Observation of Reversible Magnesium Ion Intercalation into a Spinel Oxide Host. Adv. Mater. **2015**, 27, 3377-3384. DOI: 10.1002/adma.201500083

[12] Gautam, G. S.; Canepa, P.; Urban, A.; Bo, S.-H.; Ceder, G. Influence of Inversion on Mg Mobility and Electrochemistry in Spinels. *Chem. Mater.* **2017**, 29 (18), 7918-7930. DOI: 10.1021/acs.chemmater.7b02820

[13] Bayliss, R. D.; Key, B.; Gautam, G. S.; Canepa, P.; Kwon, B. J.; Lapidus, S. H.; Dogan, F.; Adil, A. A.; Lipton, A. S.; Baker, P. J.; Ceder, G.; Vaughey, J. T.; Cabana, J. Probing Mg Migration in Spinel Oxides. *Chem. Mater.* **2020**, 32, 663-670. 10.1021/acs.chemmater.9b02450

[14] Kwon, B. J.; Yin, L.; Park, H.; Parajuli, P.; Kumar, K.; Kim, S.; Yang, M.; Murphy, M.; Zapol, P.; Liao, C.; Fister, T. T.; Klie, R. F.; Cabana, J.; Vaughey, J. T.; Lapidus, S. H.; Key, B. High Voltage Mg-Ion Battery Cathode via a Solid Solution Cr–Mn Spinel Oxide. *Chem. Mater.* **2020**, 32, 6577-6587. DOI: 10.1021/acs.chemmater.0c01988

[15] Yin, L.; Kwon, B. J.; Choi, Y.; Bartel, C. J.; Yang, M.; Liao, C.; Key, B.; Ceder, G.; Lapidus, S. H. Operando X-ray Diffraction Studies of the Mg-Ion Migration Mechanisms in Spinel Cathodes for Rechargeable Mg-Ion Batteries. *J. Am. Chem. Soc.* **2021**, 143, 10649-10658. DOI: 10.1021/jacs.1c04098

[16] Lee, J.; Dey, S.; Dutton, S. E.; Grey, C. P. Synthesis and Characterization of Magnesium Vanadates as Potential Magnesium-Ion Cathode Materials through an Ab Initio Guided Carbothermal Reduction Approach," *Ange. Chem. Int. Ed.* **2022**, 61, e202112688. DOI: 10.1002/anie.202112688

[17] Chen, T.; Gautam, G. S.; Huang, W.; Ceder, G. First-Principles Study of the Voltage Profile and Mobility of Mg Intercalation in a Chromium Oxide Spinel. *Chem. Mater.* **2018**, 30 (1), 153-162. DOI: 10.1021/acs.chemmater.7b04038

[18] Kwon, B. J.; Yin, L.; Roy, I.; Leon, N. J.; Kumar, K.; Kim, J. J.; Han, J.; Gim, J.; Liao, C.; Lapidus, S. H.; Cabana, J.; Key, B. Facile Electrochemical Mg-Ion Transport in a Defect-Free Spinel Oxide. *Chem. Mater.* **2022**, 34, 3789-3797. DOI: 10.1021/acs.chemmater.2c00237

[19] Deivanayagam, R.; Ingram, B. J.; Shahbazian-Yassar, R. Progress in development of electrolytes for magnesium batteries. *Ener. Stor. Mater.* **2019**, 21, 136-153. DOI: 10.1016/j.ensm.2019.05.028

[20] Leon, N. J.; He, M.; Liao, C. Solvation, Rational Design, and Interfaces: Development of Divalent Electrolytes. *Front. Ener. Res.* **2022**, 9, 802398. DOI: 10.3389/fenrg.2021.802398

[21] Tutusaus, O.; Mohtadi, R.; Singh, N.; Arthur, T. S.; Mizuno, F. Study of Electrochemical Phenomena Observed at the Mg Metal/Electrolyte Interface. *ACS Ener. Lett.* **2017**, 2, 224-229. DOI: 10.1021/acsenergylett.6b00549

[22] Lipson, A. L.; Han, S.-D.; Pan, B.; See, K. A.; Gewirth, A. A.; Liao, C.; Vaughey, J. T.; Ingram, B. J. Practical Stability Limits of Magnesium Electrolytes. J. *Electrochem. Soc.* **2016**, 163, A2253. DOI: 10.1149/2.0451610jes

[23] Lau, K.-C.; Seguin, T. J.; Carino, E. V.; Hahn, N. T.; Connell, J. G.; Ingram, B. J.; Persson, K. A.; Zavadil, K. R.; Liao, C. Widening Electrochemical Window of Mg Salt by Weakly Coordinating Perfluoroalkoxyaluminate Anion for Mg Battery Electrolyte. *J. Electrochem. Soc.* **2019**, 166, A1510. DOI: 10.1149/2.0751908jes

[24] Chen, S.; Ma, H.; Du, Y.; Zhang, W.; Yang, H. Y. Challenges and recent progress on anodes and their interfacial optimization towards high-performance rechargeable magnesium batteries. *Mater. Today*, **2024**, 72, 282-300. DOI: 10.1016/j.mattod.2023.12.002

[25] Lee, P. Y.; Suematsu, H.; Yano, T.; Yatsui, K. Synthesis and characterization of nanocrystalline $MgAl_2O_4$ spinel by polymerized complex method. *J. Nanopart. Res.* **2006**, 8, 911–917. DOI: 10.1007/s11051-005-9055-4

[26] Kobayashi, Y.; Ke, X.; Hata, H.; Schiffer, P.; Mallouk, T. E. Soft Chemical Conversion of Layered Double Hydroxides to Superparamagnetic Spinel Platelets. *Chem. Mater.* **2008**, 20, 2374–2381. DOI: 10.1021/cm703443q

[27] Kovanda, F.; Grygar, T.; Dorničák, V.; Rojka, T.; Bezdička, P.; Jirátová, K. Thermal behaviour of Cu–Mg–Mn and Ni–Mg–Mn layered double hydroxides and characterization of formed oxides. *App. Clay Sci.* **2005**, 28, 121-136. DOI: 10.1016/j.clay.2004.01.007

[28] Jeong, I. R.; Lee, J. H.; Song, J.; Oh, Y. S.; Cho, S. Control of structural disorder in spinel ceramics derived from layered double hydroxides. *Ceram. Inter.* **2020**, 46, 6594-6599. DOI: 10.1016/j.ceramint.2019.11.145

[29] Hirano, M.; Okumura, S.; Hasegawa, Y.; Inagaki, M. Direct precipitation of spinel type oxide $ZnGa_2O_4$ from aqueous solutions at low temperature below 90°C. *Inter. J. Inorg. Mater*. **2001**, 3, 797-801. DOI: 10.1016/S1466-6049(01)00178-7

[30] Paul, B.; Bhuyan, B.; Purkayastha, D. D.; Dhar, S. S.; Behera, S. Facile synthesis of spinel $CuCr_2O_4$ nanoparticles and studies of their photocatalytic activity in degradation of some selected organic dyes. *J. All. Com.* **2015**, 648, 629-635. DOI: 10.1016/j.jallcom.2015.07.012

[31] Greenstein, E. P.; Poeppelmeier, K. R.; Marks, L. D. Wet to Dry Controls Lanthanide Scandate Synthesis. *Inorg. Chem*. **2023**, 62, 4853–4860. DOI: 10.1021/acs.inorgchem.2c04107

[32] Pang, J.-B.; Qiu, K.-Y.; Xu, J.; Wei, Y.; Chen, J. Synthesis of Mesoporous Silica Materials via Nonsurfactant Urea-Templated Sol-Gel Reactions. *J. Inorg. Organomet. Poly.* **2000**, 10, 39-49. DOI: 10.1023/A:1009404415925

[33] Zheng, J.-Y.; Pang, J.-B.; Qiu, K.-Y.; Wei, Y. Synthesis and characterization of mesoporous titania and silica–titania materials by urea templated sol–gel reactions. *Micropor. Mesopor. Mater.* **2001**, 49, 189-195.

[34] Son, S.-B.; Gao, T.; Harvey, S. P.; Steirer, K. X.; Stokes, A.; Norman, A.; Wang, C.; Cresce, A.; Xu, K.; Ban, C. An artificial interphase enables reversible magnesium chemistry in carbonate electrolytes. *Nat. Chem.* **2018**, 10, 532-539. DOI: 10.1038/s41557-018-0019-6

[35] Liu, X.; Du, A.; Guo, Z.; Wang, C.; Zhou, X.; Zhao, X.; Sun, F.; Dong, S.; Cui, G. Uneven Stripping Behavior, an Unheeded Killer of Mg Anodes. *Adv. Mater.* **2022**, 34, 2201886. DOI: 10.1002/adma.202201886

[36] Kwon, B. J.; Lau, K.-C.; Park, H.; Wu, Y. A.; Hawthorne, K. L.; Li, H.; Kim, S.; Bolotin, I.L.; Fister, T. T.; Zapol, P.; Klie, R. F.; Cabana, J.; Liao, C.; Lapidus, S. H.; Key, B.; Vaughey, J.T. Probing Electrochemical Mg-Ion Activity in MgCr2-x-VxO4 Spinel Oxides. *Chem. Mater.* **2020**, 32, 3, 1162-1171. DOI: 10.1021/acs.chemmater.9b04206

[37] Kobayashi, H.; Fukumi, Y.; Watanabe, H.; Iimura, R.; Nishimura, N.; Mandai, T.; Tominaga, Y.; Nakayama, M.; Ichitsubo, T.; Honma, I.; Imai, H. Ultraporous, Ultrasmall $MgMn_2O_4$ Spinel Cathode for a Room-Temperature Magnesium Rechargeable Battery. *ACS Nano*. **2023**, 17 (3), 3135–3142. DOI: 10.1021/acsnano.2c12392

[38] Sone, K.; Hayashi, Y.; Mandai, T.; Yagi, S.; Oaki, Y.; Imai, H. Effective 3D open-channel nanostructures of a $MgMn_2O_4$ positive electrode for rechargeable Mg batteries operated at room temperature. *J. Mater. Chem. A*. **2021**, 9, 11, 6851-6860. DOI: 10.1039/D0TA07974J

[39] Kobayashi, H.; Samukawa, K.; Nakayama, M.; Mandai, T.; Honma, I. Promoting Reversible Cathode Reactions in Magnesium Rechargeable Batteries Using Metastable Cubic $MgMn_2O_4$ Spinel Nanoparticles. *ACS Appl. Nano Mater.* **2021**, 4, 8328–8333. DOI: 10.1021/acsanm.1c01519

[40] Jung, Y.-S.; Yoon, W.-L.; Seo, Y.-S.; Rhee, Y.-W. The effect of precipitants on Ni-$Al_2O_3$ catalysts prepared by a co-precipitation method for internal reforming in molten carbonate fuel cells. *Catal. Comm.* **2012**, 26, 103-111. DOI: 10.1016/j.catcom.2012.04.029

[41] Han, X.; Yu, Y.; He, H.; Zhao, J.; Wang, Y. Oxidative steam reforming of ethanol over Rh catalyst supported on $Ce_{1-x}La_xO_y$ (x = 0.3) solid solution prepared by urea co-precipitation method. *J. Power Sources*. **2013**, 238, 57-64. DOI: 10.1016/j.jpowsour.2013.03.032

[42] Zhang, R.; Arthur, T. S.; Ling, C.; Mizuno, F. Manganese dioxides as rechargeable magnesium battery cathode; synthetic approach to understand magnesiation process. *J. Power Sources*. **2015**, 282, 630-638. DOI: 10.1016/j.jpowsour.2015.02.067

[43] Kaneko, T.; Fujihara, Y.; Kobayashi, H.; Sodeyama, K. First-principles study of the reconstruction of $MgM_2O_4$ (M = Mn, Fe, Co) spinel surface. *App. Surf. Sci.* **2023**, 613, 156065. DOI: 10.1016/j.apsusc.2022.156065

[44] Vaughey, J. T.; Trask, S.; Poeppelmeier, K. Synthesis as a Design Variable for Oxide Materials. *Electrochem. Soc. Interface*. **2021**, 30, 53-58. DOI: 10.1149/2.F08211IF